47th AIAA Aerospace Sciences Meeting Including The New Horizons Forum and Aerospace Exposition
5 - 8 January 2009, Orlando, Florida

AIAA 2009-22

Dynamics of a Longitudinally Forced, Bluff Body Stabilized Flame

Tim Lieuwen[1], Dmitriy V Plaks[2], and Dong-Hyuk Shin[2]
Georgia Institute of Technology, Atlanta, GA, 30318

Ulises M. Mondragon[3], Christopher T. Brown[4] and Vincent G. McDonell[5]
Energy Research Consultants, Laguna Hills, CA, 92653-1422, USA

and

Barry V. Kiel[6]
Air Force Research Laboratory, Wright Patterson AFB, OH 45433, USA

This paper describes an investigation of the response of bluff body stabilized flames to harmonic oscillations. This problem involves two key elements – the excitation of hydrodynamic flow instabilities by acoustic waves, and the response of the flame to these harmonic flow instabilities. In the present work, data were obtained with inlet temperatures from 311 K to 866 K and flow velocities from 38 m/s to 170 m/s. These data show that the flame front response at the acoustic forcing frequency first increases linearly with downstream distance, then peaks and decays. The corresponding phase decreases linearly with axial distance, showing that wrinkles on the flame propagate with a nearly constant convection velocity. These results are compared to those obtained from a theoretical solution of the *G*-equation excited by a harmonically oscillating, convecting disturbance. This kinematic model shows that the key processes controlling the response are 1) the anchoring of the flame at the bluff body, 2) the excitation of flame-front wrinkles by the oscillating velocity, and 3) flame propagation normal to itself at the local flame speed. The first two process control the growth of the flame response and the last process controls the decay. These predictions are shown to describe the key features of the measured flame response characteristics.

Nomenclature

A	=	flame area
d	=	bluff body diameter
D	=	burner depth
f	=	frequency
f_o	=	forcing frequency
f_{BvK}	=	Bénard/von Kármán instability frequency
f_{KH}	=	Kelvin-Helmholtz frequency
G	=	isoscalar contour variable
h_R	=	heat of reaction
I_t	=	edge detection threshold
K	=	non-dimensionalized convective disturbance velocity
L	=	flame position
L_f	=	average spatial flame extent
Q	=	heat release
Re	=	Reynolds number

[1] Associate Professor, School of Aerospace Engineering, 270 Ferst Dr, AIAA Associate Fellow.
[2] Graduate Research Assistant, School of Aerospace Engineering, 270 Ferst Dr, AIAA Student Member
[3] Sr. Research Engineer, 23342 South Point Drive, Suite E, Laguna Hills, CA, 92653
[4] Research Manager, 23342 South Point Drive, Suite E, Laguna Hills, CA, 92653
[5] Senior Scientist, 23342 South Pointe Dr, Suite E, Laguna Hills, CA, 92653, Senior AIAA Member
[6] Augmentor Technical Leader, AFRL/PRTC, Bldg 490, Room 109, Senior AIAA Member

S_L = laminar flame speed
S_u = flame speed
t = time
W = burner width
u = flow velocity
u' = unsteady flow velocity
u_0 = mean flow velocity
u_c = convective velocity of a disturbance
u_n = flow velocity normal to the flame
u_t = flow velocity tangential to the flame
u_θ = velocity amplitude associated with a vortex
x = position along mean flow direction
y = position perpendicular to mean flow direction
β = parametric flame front angle
γ = vortex decay rate
ε = non-dimensionalized disturbance amplitude
θ = flame front angle
λ_c = convective wavelength, = u_o/f_0
ν = spatial cutoff frequency
ρ = density
ω = disturbance frequency

I. Introduction

This paper describes an investigation of the response of bluff body stabilized flames to harmonic oscillations. Prior studies have shown that this problem involves feedback between acoustic oscillations, hydrodynamic flow instabilities associated with the shear layer and wake, and unsteady heat release[1,2,3,4]. This problem involves two key elements – the excitation of hydrodynamic flow instabilities by acoustic waves, and the response of the flame to these harmonic flow instabilities, as illustrated in Figure 1. These two elements are discussed briefly next.

The bluff-body flow-field consists of a boundary layer, a separated shear layer and a wake. The velocity field of the separated shear layer and the wake has an inflexion point, rendering both susceptible to hydrodynamic instabilities. The wake mode, referred to here as the Bénard/von Kármán (BvK) instability, leads to alternate shedding of vorticity from opposite sides of the bluff body and a sinuous wake structure. The frequency of this absolute instability, f_{BVK}, scales as u_o/d, where u_o and d denote the mean flow velocity and bluff body width, respectively. The shear layer instability, or Kelvin-Helmholtz (KH) instability, is a convective instability associated with the amplification of disturbances, leading to vortex rollup and pairing of the separating shear layer. The frequency of the most amplified KH instability mode is different than that of the BvK, because the relevant length scale is the shear layer thickness rather than the bluff body size. As such, the KH instability frequency is much larger than the BvK instability for high Reynolds number flows; e.g., relations from Ref. 5 lead to $f_{KH} = 0.0235*f_{BVK}*Re^{0.67}$. Under the influence of harmonic excitation, the separated shear layer rolls up into vortices with a frequency commensurate with the frequency of excitation[6]. In addition, due to nonlinear interactions, velocity fluctuations occur at sum and difference frequencies of the forcing frequency and its harmonics[6].

As discussed in the next section, due to the apparent suppression of the BvK instability in flames with burned to unburned gas temperature ratios greater than about two[7], the shear layer instability is of particular significance in controlling the dynamics of acoustically excited, bluff body flames. Heat release substantially influences the flow disturbances which are, in turn, disturbing the flame[8,9,10]. As an example of such an influence, consider the stabilization of the wake mode instability by volume dilatation, as discussed by Ref. 7. In the absence of any combustion (equivalent to dilatation ratio of one), the wake mode instability is clearly seen. However as the dilatation ratio increases, the strength of the vortices decreases, until at a dilatation ratio of about two, the wake mode instability is apparently absent.

Fundamental studies of vortex-flame interactions have shown that the nature of the flow changes substantially with the amplitude of vorticity perturbation[11,12,13]. For low vortex strengths, the flame is wrinkled with amplitude proportional to the ratio of u_θ/S_L, where u_θ denotes the velocity amplitude associated with the vortex and S_L the laminar flame speed. The amplitude of the vortex decreases through the flame due to volume dilatation and the large diffusivity of the products. Furthermore, if the flow and flame are nominally normal to each other, the baroclinic

term is zero. As the amplitude of the vortex increases, the flame becomes highly wrinkled to the point that vorticity can also be produced/destroyed by baroclinic processes, i.e., very strong vortices distort the flame to such an extent that they change the sign of the baroclinically generated vorticity along the corrugated flame sheet. However, one key difference between the present investigation and the above cited studies is the fact that the flame is nominally at an angle to the flow, so that baroclinic vorticity is present even in the nominal, unforced case. Nonetheless, this discussion illustrates the complications that can arise between shear generated vorticity that has its own dynamics (e.g., rollup, pairing, growth, etc.), viscous diffusion, volume dilatation, and baroclinic processes.

Because of the strong interactions between the flame and flow field, studying the problem of acoustic wave interactions with bluff body flames does not allow breaking this problem into the more simple sub-problems, such as "direct" acoustic wave interactions with the flame (because the flame response is dominated by the vorticity fluctuations excited by the acoustics), or acoustic wave interactions with a non-reacting bluff body flow field (because volume dilatation associated with the flame fundamentally changes the nature of the interaction).

The second element described in the first paragraph is the response of the flame to harmonic excitation. Substantial contributions have been made towards understanding the interaction between harmonic waves and premixed flames, and several issues have been identified as significant, such as stabilization dynamics and the spatial character of the disturbance field[14,15]. A number of prior studies have characterized the interaction of flames with harmonic waves arising due to both acoustic waves[16] and also convecting, vortical disturbances[17, 18]. The dynamics of the flame is controlled by flame kinematics, i.e., the propagation of the flame normal to itself at the local burning velocity, and the flow field that the flame is locally propagating into. This is mathematically described by the so-called G-equation[19]:

$$\frac{\partial G}{\partial t} + \vec{u} \cdot \nabla G = S_L \left| \nabla G \right| \tag{1}$$

In this equation, the flame position is described by the parametric equation $G(\vec{x},t) = 0$. Also, $\vec{u} = \vec{u}(\vec{x},t)$ and S_L denote the flow field just upstream of the flame and laminar flame speed, respectively. In the unsteady case, the flame is being continually wrinkled by the unsteady flow field, $\vec{u}'$. The action of flame propagation normal to itself, the term on the right side of Eq. (1), is to attempt to smooth these wrinkles out. As such, a wrinkle created at one point of the flame due to a velocity perturbation propagates downstream and diminishes in size due to flame propagation. Indeed, the dynamical interaction between the driving (acoustic oscillations) and the damping (restoration property of the flame) can lead to a range of effects depending upon the relative values of the flow oscillations and flame speed. This manifests itself through both local influences upon the flame topology (e.g., cusping, amplitude of corrugation, pocket formation), and global influences upon the overall unsteady heat release response of the flame.

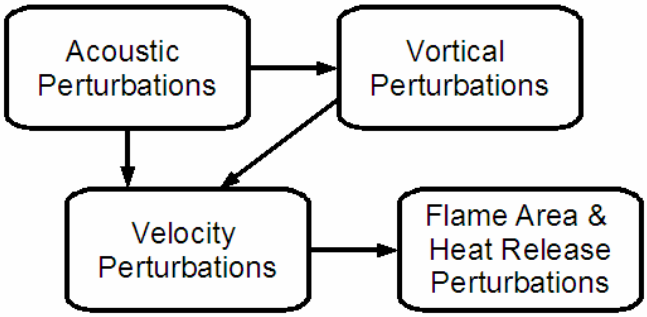

Figure 1. Physical processes by which longitudinal and transverse flow oscillations lead to flame area (and hence heat release) oscillations.

The objective of this study is to characterize this relationship between acoustic, vortical and flame sheet fluctuations. It extends prior measurements and analysis by the Georgia Tech group from much lower velocity and Reynolds number flames to much higher velocity flames.[20-22]

II. Experimental Facility, Data Processing and Modeling Approach

A. Experimental Setup and Data Post-Processing

Experiments are conducted in a premixed, atmospheric test rig (see Figure 2) operated in both a vitiated and non-vitiated mode[23]. The test section is 76.2 mm x 127 mm with a triangular bluff body of 31.75 mm wide and 50.8 mm high. Air enters at the base of the setup and is mixed with natural gas in the next chamber. After the mixture burns in the vitiator, dilution air is added and the flow passes through a pebble bed. Natural gas is added immediately after the pebble bed section. The flow passes through a converging section and a honeycomb flow straightener before entering the test section. The flow velocity at the bluff body varies from 18 m/s to 170 m/s and the inlet temperature into the test section varies from 311 K (non-vitiated) to 866 K, see Table 1. Fuel concentration profiles were measured just upstream of the bluff body and spatial non-uniformities are less than 2% at 15 m/s and 20% at 190 m/s (the latter case is vitiated).

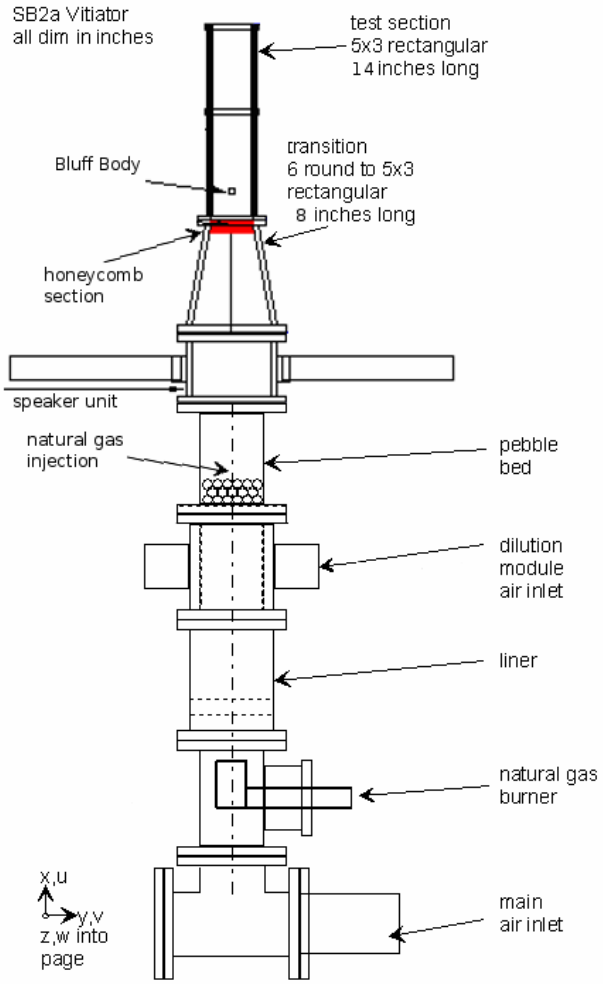

Figure 2. Schematic of the experimental rig.

a) Design

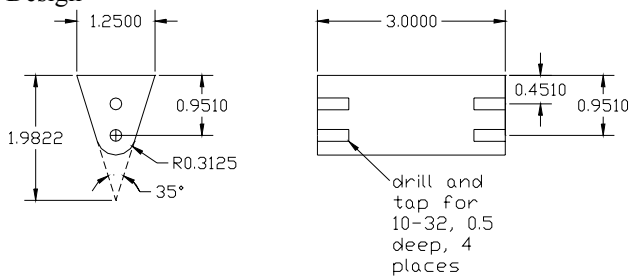

b) Installed in Test Section

Figure 3. Schematic and photograph of bluff body used in these measurements.

Longitudinal oscillations are excited with a driver section, installed upstream of the test section. These drivers consist of four 100W Galls Speakers powered by two Samson Audio Servo 200 Power amplifiers. The signal is generated by a function generator. Acoustic signature from the rig was documented using a PCB dynamic pressure transducer and oscilloscopes and labview.

Flame dynamics are determined from direct flame luminosity, recorded with a Vision Research Phantom 7.2 black and white high speed video camera. The visible (>330 nm) broadband light emission was recorded using a Nikon 35-70mm zoom lens with a f-stop of 3.3. Typically, the exposure time was 328 microseconds and recording rates of 1000 and 3000 frames per second were used.

Table 1. Summary of flow conditions and the chosen threshold values. Each experiment set is conducted at two excitation amplitudes of 6V and 12V speaker excitation voltage.

Air Flow Rate (kg/s)	Flow Velocity at Bluff Body (m/s)	Air Flow Temperature Upstream of Bluff Body (K)	Edge Detection Threshold
0.14	18	294	0.25
0.14	38	644	0.27
0.18	51	644	0.20
0.23	63	644	0.13
0.27	76	644	0.13
0.32	89	644	0.13
0.36	101	644	0.45
0.41	114	644	0.45
0.45	126	644	0.45
0.45	170	866	0.45

B. Model Development

The flame position is modeled using the G equation, described in the Introduction section. Assuming that the flame position is a single valued function of the transverse coordinate, the instantaneous flame position can be written as:

$$G(x,y,t) = L(x,t) - y = 0$$

Assuming a two dimensional flame, the instantaneous flame position, L, is given by:

$$\frac{\partial L}{\partial t} + u\frac{\partial L}{\partial x} - v = S_L\sqrt{\left(\frac{\partial L}{\partial x}\right)^2 + 1} \qquad (2)$$

The coordinate system is shown in Figure 4. The G equation describes the spatial and temporal distributions of the flame position that can be related directly to the area. In this formulation, the effect of transverse and longitudinal velocity perturbations on the flame are captured through the (*u, v*) terms.

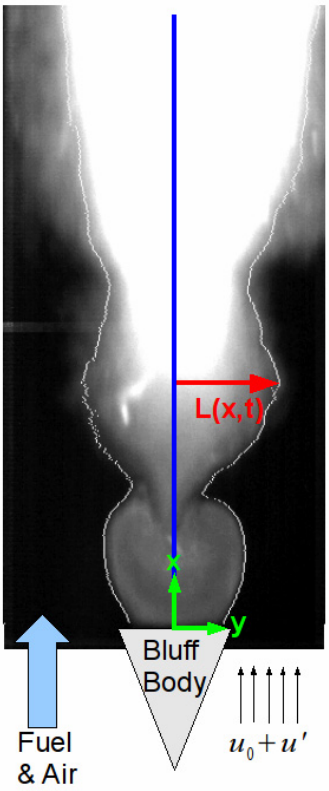

Figure 4. Schematic of flame model used to compare and predict experimental results.

It is known that acoustic excitation results in a train of convecting vortices generated in the bluff body shear layer that decay in the downstream direction.[24] As such, the axial velocity field is described by the equation (the associated transverse velocity components are then determined by the continuity equation)[22]:

$$u(x,y,t) = u_0(x,y) + u'\cos(\omega(t - x/u_c))e^{-\gamma x} \tag{3}$$

The associated flame response is then influenced by this disturbance field through four parameters: 1) the amplitude of disturbance, $\varepsilon = u'/u_o$, 2) the frequency of disturbance, ω, 3) the convective velocity of the disturbance, u_c (in calculations, it is non-dimensionalized by the mean velocity, $K = u_c/u_o$, and 4) the decay rate of the vortices, γ. These parameters themselves are influenced by geometry and flame angle.

In addition, there are two additional parameters that influence the flame response that are directly associated with the flame itself. The first is the angle of the flame front with respect to the mean velocity, θ, parameterized here by $\beta=\tan(\theta)$. The second parameter is the response of the flame attachment point to the excitation. Based upon the visualization results obtained, it has been assumed that the flame sheet remains firmly attached to the bluff body separation point and does not oscillate in response to the excitation. As such, this latter parameter drops out.

Because the G equation is a nonlinear partial differential equation with special properties, including being non-conservative and having the propensity to form discontinuities in derivatives, special computational approaches are required for its solution. In particular, a robust numerical scheme is necessary which can accurately capture the formation of sharp gradients and cusps in the distorted flame front. The computational approach utilized here discretizes spatial derivatives using a Weighted Essentially Non-Oscillatory (WENO) scheme developed for Hamilton-Jacobi equations[25]. This scheme is uniformly fifth order accurate in space in the smooth regions and third order accurate in discontinuous regions. Derivatives at the boundary nodes are calculated using fifth order accurate

upwind-differencing schemes so that only the nodes inside the computational domain are utilized. A Total Variation Diminishing (TVD) Runge-Kutta scheme[26], up to third order accurate, is used for time integration.

C. Image Processing

High speed, line-of-sight movies were obtained of the acoustically forced flames. Typical images at several flow conditions are shown in Figure 5. In order to determine the dynamics of the flame edge, given by $L(x,t)$ in Eq. (2), it is necessary to extract the flame edges. This process is complicated by the integration over the line of sight in the image, which causes the edge of the flame in each image to grow increasingly diffuse with downstream distance, due to the growing three-dimensionality of the flame front.

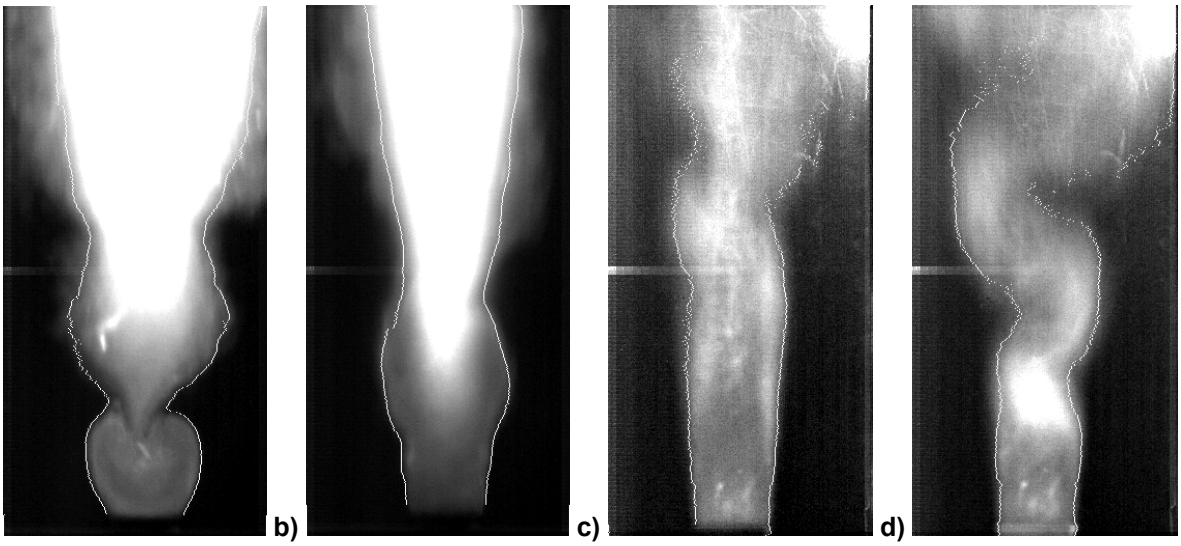

Figure 5. Luminosity flame images and their calculated flame edges at various flow conditions: a) 18.4 m/s, 294K; b) 38.0 m/s, 644K; c) 127 m/s, 644K; d) 170 m/s, 866K. All cases have a 12V excitation voltage.

These points can be seen in Figure 6, which illustrates a typical flame image and transverse cuts of the smoothed intensity profile at two axial locations. It can be seen that near the bluff body, there is an abrupt rise in image intensity associated with the edge of the flame. Farther downstream this edge becomes increasingly diffuse. As such, the defined flame edge increasingly becomes a function of the threshold value with downstream axial distance.

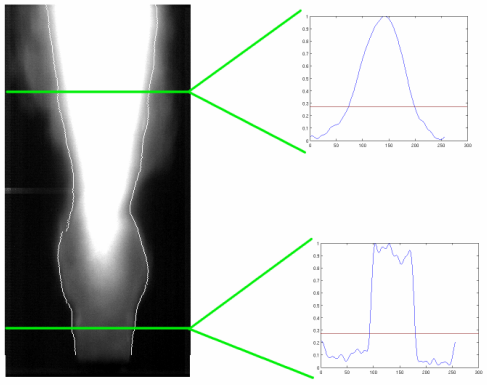

Figure 6. Image intensity at two axial locations. The flame edge location is defined where the intensity crosses the threshold value, I_t. Flow velocity is 38.0 m/s at 644K and 12V excitation voltage.

We next discuss the specific procedure used for flame edge extraction. First, the data is smoothed with an ideal low-pass filter having a spatial cutoff wavelength of v = 0.662 m^{-1}. Since image intensity changes with downstream distance, the image is normalized to vary between zero and unity at each axial location. Then, the flame edge, $L(x,t)$ is defined as the point where the intensity crosses some defined threshold level, I_t. Note that two flame edges are

extracted, associated with the right and left flame branches.

This process is repeated for all rows in a single image and again for all images in a movie and results in a time series for every row (x-direction) in an image, as shown in Figure 7a. These time domain data are also converted into the frequency domain at each axial location by obtaining the Fourier transform at each axial location, see Figure 7b. Note the spike at the forcing frequency, f_0 = 250Hz. The resulting axial dependence of the flame response magnitude and phase at the forcing frequency are shown in Figure 8.

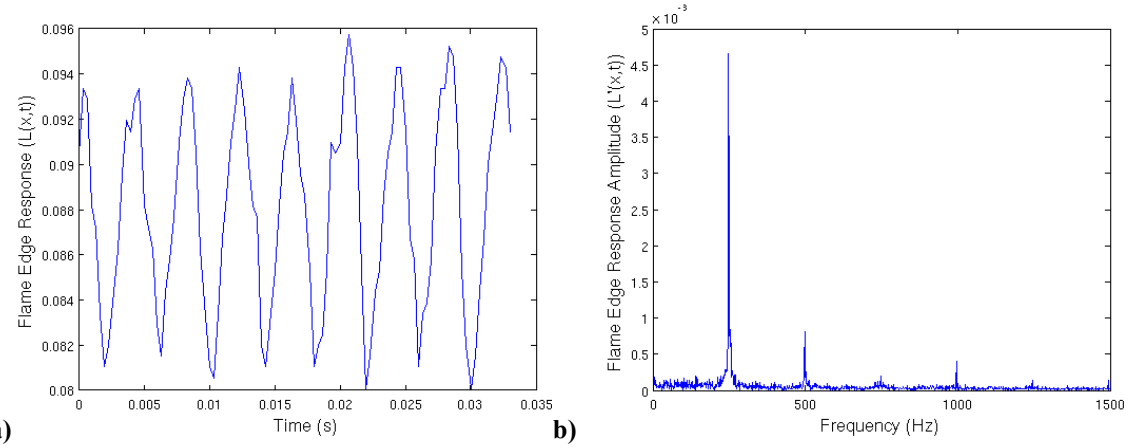

Figure 7. a) Time series of flame position using I_t = 0.27 at axial location of x/λ_c = 0.47. b) Corresponding spectrum, showing strong response at 250 Hz forcing frequency. Flow conditions: 38 m/s mean flow velocity, 644 K approach temperature, and 12V excitation voltage.

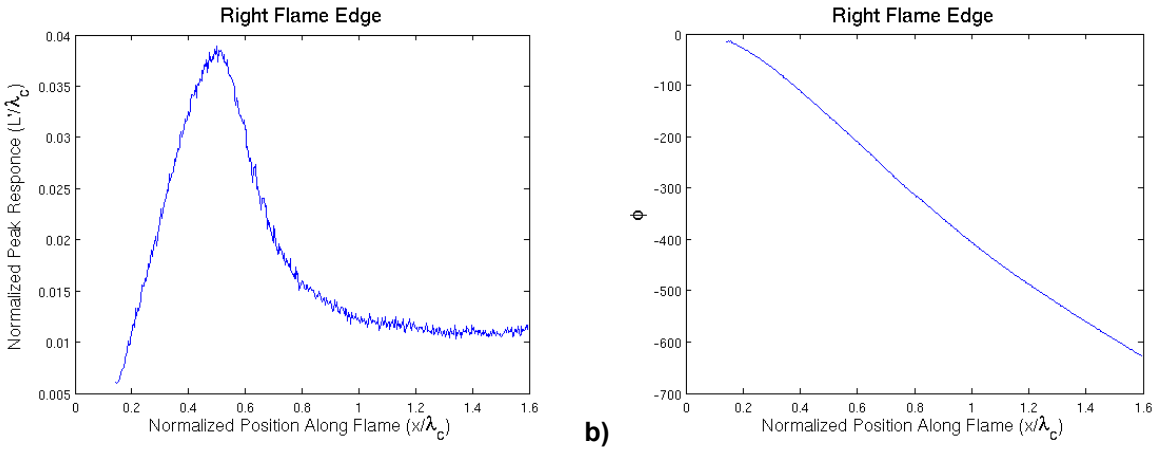

Figure 8. a) Normalized flame edge response amplitude at the forcing frequency as a function of normalized downstream distance. b) Flame edge response phase at the forcing frequency as a function of downstream frequency. Flame edge response amplitude, phase and downstream distance are normalized by the convective wavelength, λ_c. Flow conditions: 38 m/s mean flow velocity, 644 K approach temperature, 12V excitation voltage and I_t = 0.27.

In order to ensure quality of the data, several techniques are used for checking data validity. First, each point is checked to make sure it lies further than 10 pixels away from the image border (due to the nature of the data and the edge detection algorithm, many erroneous points default to a value at the image border). If such a point is encountered away from top and bottom image boundaries (i.e., near the center of the flame) the gap is filled by interpolating between nearby points. The data is discarded when such events occur in the nearfield (starting with x = *0* and moving along the flame until a first valid point is encountered) of the bluff body and far downstream (starting at the top end of the image and moving down until a first valid point is encountered) where the magnitude of the fluctuations is low. Furthermore, the number of discontinuities and the mode of the time series are computed for each x-location. If the number of discontinuities is greater than 1.5% of the total number of points in the time series

at that location, or the mode is less than 12% or greater than 50% (left edge) or less than 50% or greater than 95%, the result is not reported.

Second, the coherence between the left flame edge and the right flame edge is calculated at the forcing frequency. Only axial points where the coherence exceeds 0.9 are reported. Typical coherence data is shown in Figure 9. It shows that coherence values are smallest near the bluff body and far downstream, where the magnitude of flame sheet fluctuations is smallest and, therefore, random noise effects are most prominent. It also shows that coherence values generally increase as flow velocities decrease and as the amplitude of excitation increases.

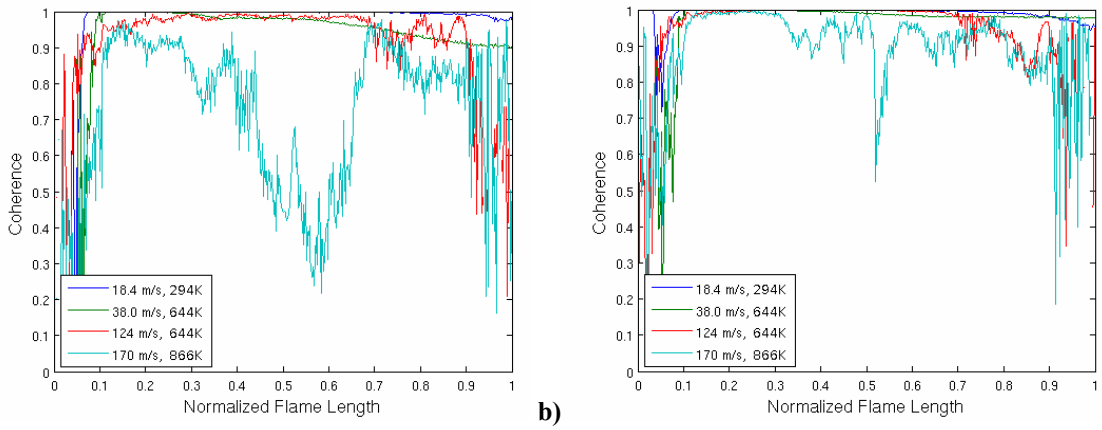

Figure 9. Coherence of the left flame branch to the right flame branch at several flow conditions and a) 6V and b) 12V excitation voltage. In general, coherence is lower at lower excitation voltage. Flow conditions: 38 m/s mean flow velocity, 644 K approach temperature, and 12V excitation voltage.

These results depend upon threshold level, I_t. This sensitivity is illustrated in Figure 10 and Figure 11. Figure 10a shows the axial dependence of the flame response magnitude at the forcing frequency at several threshold values. It shows, as expected, that all the results converge in the bluff body nearfield, where the flame is close to two-dimensional. The curves diverge with distance downstream. Next, it shows that low and high threshold values result in the largest and smallest magnitude, respectively, of fluctuations. However, the curves have similar qualitative character, as will be discussed in the next section. Figure 10b shows the corresponding axial phase dependence. This result shows significantly less phase sensitivity upon threshold value, except for the highest threshold case.

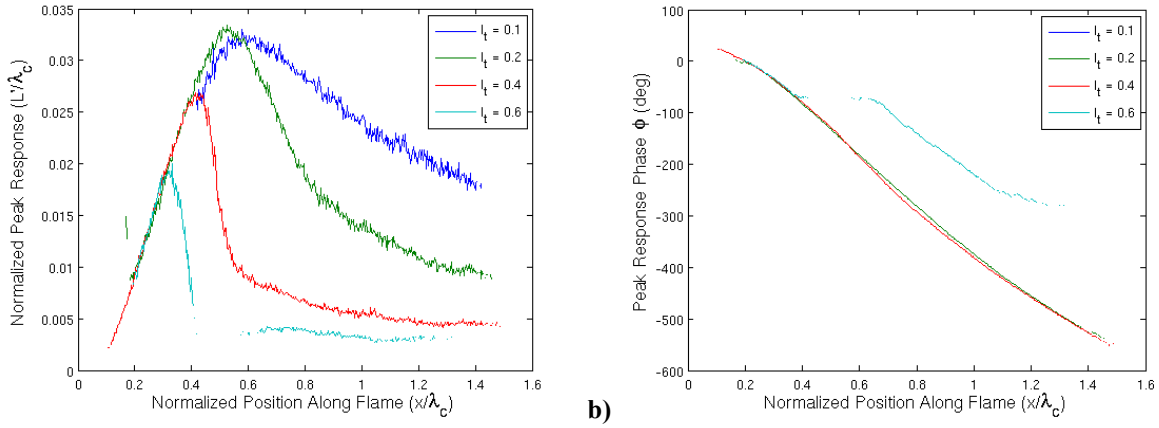

Figure 10. a) Dependence of flame edge response amplitude on threshold value choice, I_t. The initial rise slope is the same in all four cases but the peak value and location as well as the decay slope all differ. b) Dependence of flame edge response phase on threshold value choice, I_t. In three of the four cases, the general behavior of the curves is nearly identical, including the slope, which is related to the convective velocity. Flow conditions: 38 m/s mean flow velocity, 644 K approach temperature, and 12V excitation.

Figure 11 shows the sensitivity of the maximum flame edge response (i.e. maximum of L'/λ_c in Figure 10a) to the threshold value, I_t. For some flow conditions, I_t has little impact on the maximum flame edge response while for other flow conditions the maximum flame edge response value is very sensitive to the threshold value choice. Results presented in the next section use different threshold values for different flow conditions, shown in Table 1.

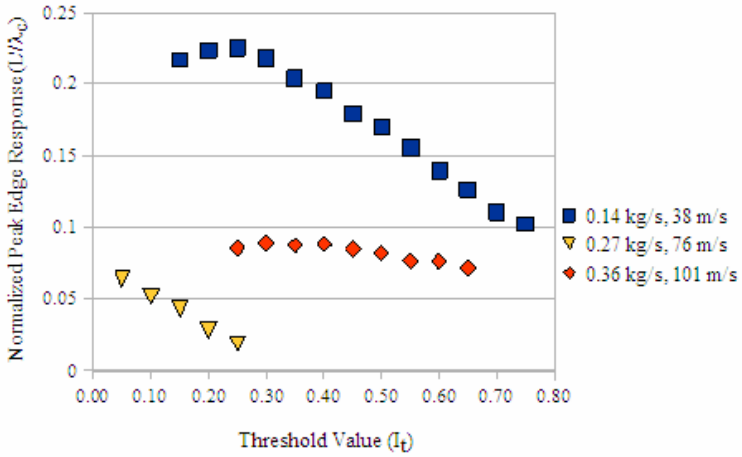

Figure 11. Variation of the peak flame edge response amplitude as a function of threshold value at three different flow conditions.

III. Experimental Results and Discussion

Typical characteristics of flame-front position spectra (both amplitude and phase), under the influence of acoustic excitation are shown in Figure 12. The convective wavelength of the flame front disturbances, $\lambda_{cf}=u_o/f_o$, (where u_o is the mean flow velocity) equals the distance a disturbance propagating at the mean flow velocity travels in one acoustic period. Figure 12 shows the entire spectrum of the flame response at seven downstream locations. The envelope of the flame response at $f = f_o$ is also drawn. Close to the bluff body (located at $y/\lambda_c=0$), the flame responds mainly at the frequency of excitation (f_o). Moving downstream, the response at $f = f_o$ first grows, reaches a maximum, and then decreases. This behavior is due to the growth and decay of the underlying flow structures as well as the propagation of the flame, which tends to smooth out the wrinkles. These results are quite similar to our observations on lower velocity flames.[22]

The spectrum also exhibits a monotonic increase in broadband fluctuations with downstream distance. This reflects the random flapping of the flame brush, which increases in magnitude with downstream axial distance.

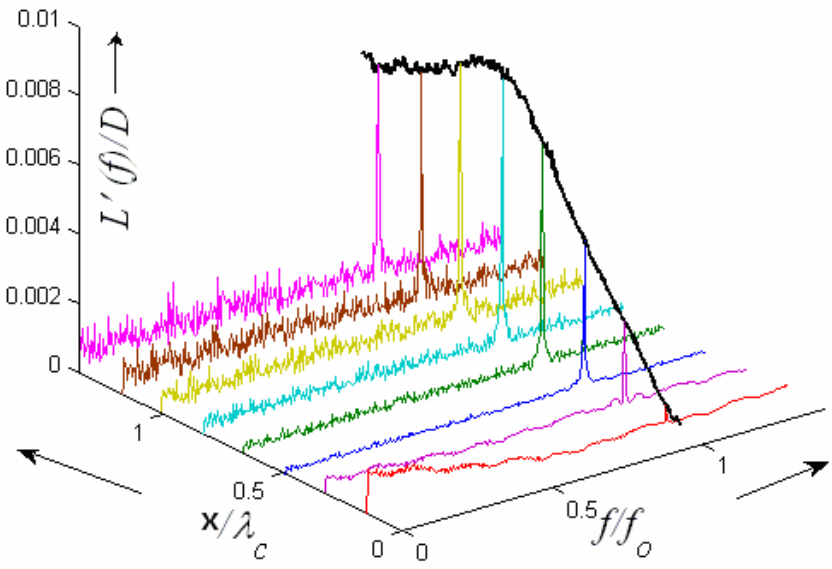

Figure 12. Spectrum of flame sheet fluctuations, *L'(x,f)* at different downstream locations (18.4 m/s, non-vitiated). The *x*-coordinate is the downstream distance with $x = 0$ located at the bluff body trailing edge and f_o is the acoustic forcing frequency.

Figure 13 and Figure 14 overlay a number of similar plots at different velocities, excitation amplitudes, and flame temperature ratios. Given the dependence of these magnitude curves to threshold level, quantitative comparison between results at different conditions, such as flow velocity, should not be attempted.

Most prominently, all curves show essentially the same qualitative behavior for both gain and phase. The gain results increase linearly in the bluff body nearfield, peak farther downstream, and then decay. The decay rate varies strongly among the different curves, being lowest in the $u_o = 50.7$ m/s case but, again, its dependence upon I_t should be noted. The phase results are essentially on top of each other, showing that the phase depends primarily upon downstream location and axial flow velocity (both effects captured in the parameter x/λ_c). The slope of these phase curves, $\Delta\phi/\Delta(x/\lambda_c) = -568$ deg and -547 deg for the 6V and 12V cases, respectively. Since phase is arbitrary, it is set to zero at $x/\lambda_c = 0.2$ where there is good flame response (there is little flame response near $x = 0$, rending large phase uncertainties)

The strong effect of axial velocity in scaling the gain results should also be emphasized. In the lowest velocity cases, the entire axial dependence of the gain can be seen (rise, peak, then decay). At the highest flow velocities, only the spatial growth region is seen. This demonstrates that the appropriate axial viewing window needed to completely characterize the flame's spatio-temporal dynamics increases linearly with flow velocity (and inversely with frequency, for related reasons).

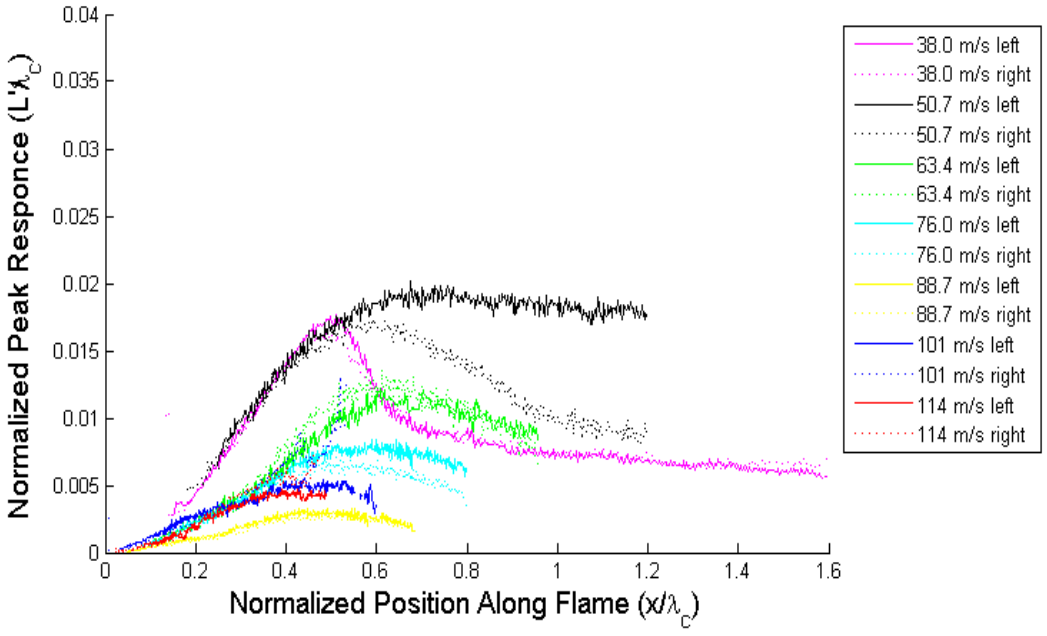

a)

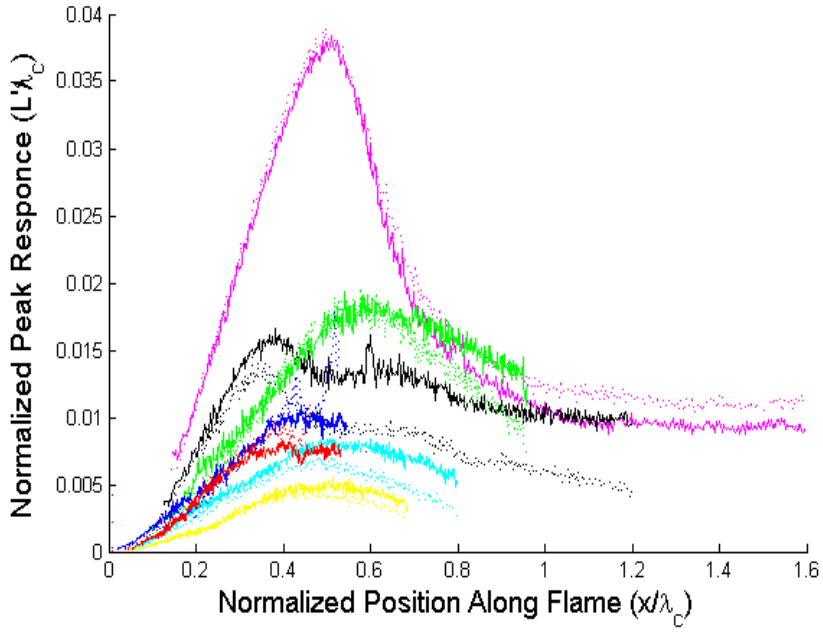

b)

Figure 13. Effect of flow velocity on peak flame response at 6V (a) and 12V (b) excitation voltage at an inlet temperature of 644 K. The *x*-coordinate is the downstream distance with $x/\lambda_c = 0$ located at the bluff body trailing edge. The left flame edge is represented by a solid line and the right flame edge is represented by a dashed line.

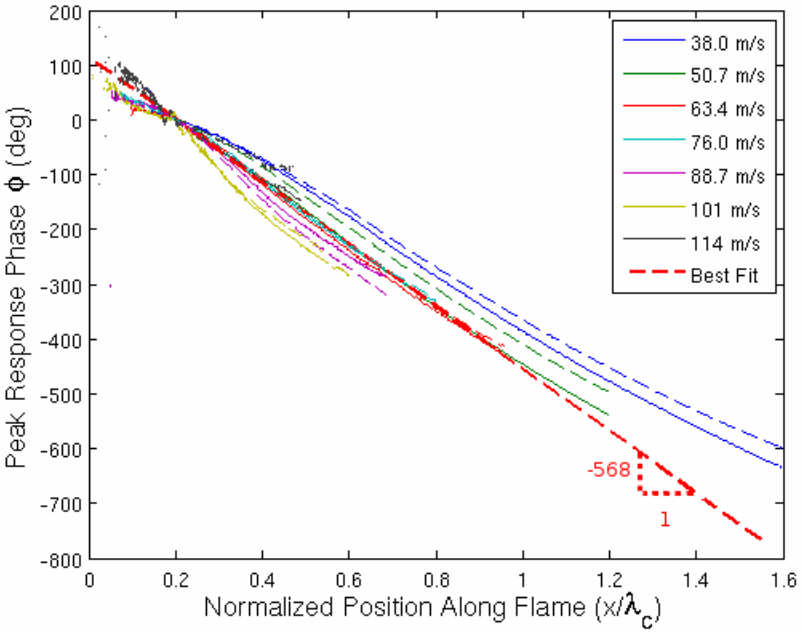

a)

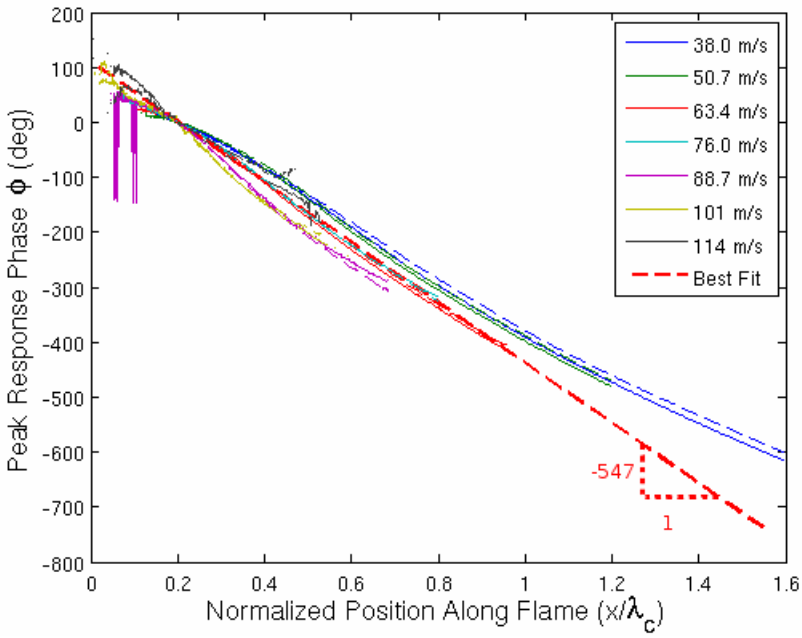

b)

Figure 14. Effect of flow velocity on phase at 6V (a) and 12V (b) excitation voltage at an inlet temperature of 644 K. The *x*-coordinate is the downstream distance with $x/\lambda_c = 0$ located at the bluff body trailing edge. The left flame edge is represented by a solid line and the right flame edge is represented by a dashed line. The best fit line is a red dashed line with the slope as indicated. The phase plots are matched for comparison at $x/\lambda_c = 0.2$.

Finally, by comparing the results for a given condition at the two different excitation amplitudes, it can be seen that the flame response increases with disturbance amplitude although not necessarily in a linear manner. This can be seen from Figure 15 which replots these same data, but normalizes the y-axis by amplitude of excitation. Note that the data collapses in the near field, but diverges in the farfield.

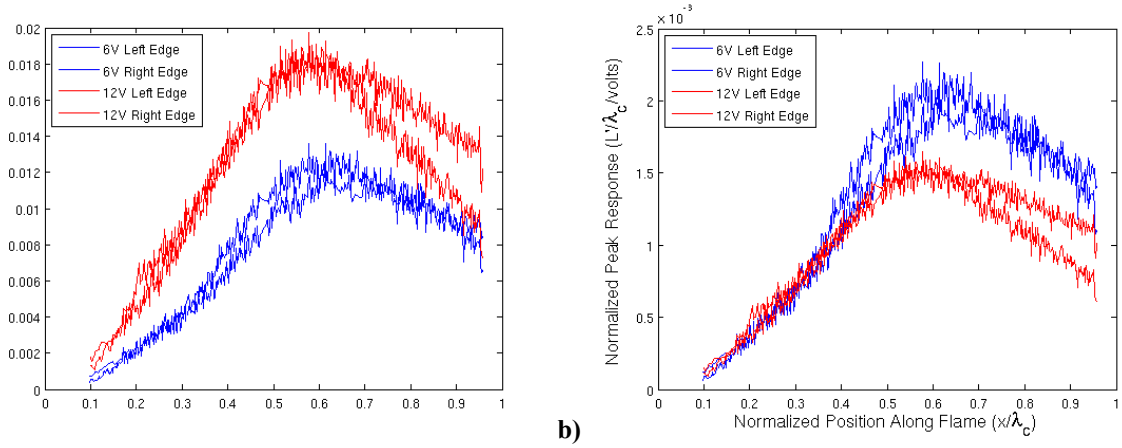

a) b)

Figure 15. Normalized amplitude plot that compares two different excitation voltages at the same flow velocity of 63 m/s where a) raw data and b) is after normalization of the amplitude by the excitation voltage to the speakers.

D. Comparison with Model

The basic solution characteristics of the G equation will next be discussed. This discussion closely follows our earlier publication by Shanbhogue, et al[22]. A key length scale is the convective wavelength, u_o/f. For low amplitude disturbances, $\varepsilon << 1$, and/or small axial distance, $x/\lambda_c << 1$, nonlinear effects are negligible and the linear and amplitude scaled nonlinear results converge, as illustrated in Figure 15. However, for large ε or x/λ_c values, the flame wrinkles are damped out by flame propagation normal to itself. Linear calculations accurately describe the flame response features in the $x/\lambda_c << 1$ region, but nonlinear effects are needed to describe the monotonic reduction in amplitude of flame response at large downstream distances. This result illustrates the intrinsic nonlinearity of the problem – a linearized solution can only describe the nearfield flame dynamics and not its full response.

Model predictions were generated for similar conditions as the data. Gain comparisons are meant to be qualitative, as the quantitative measured results are a function of I_t. Performing these calculations requires specifying the values of all the model parameters described earlier (see Eq. (3)); e.g., β, ε, γ, ω and K. The following procedure was used for this comparison: the value of the frequency ω was determined from the known forcing frequency, β was determined from the flame images in the unforced case, and K was determined from analysis of the convection velocity of the flame wrinkle. Estimates of ε and γ require, however, direct velocity measurements which were not available – however, the primary influence of these variables is upon the peak value and decay rate of the flame response magnitude, both quantities which cannot be quantitatively compared to the data.

Figure 16a overlays a number of gain and phase response curve predictions for a range of disturbance amplitude (ε), decay rate (γ) and flame angle (β) values. Notice that there are three families of color coded curves, each corresponding to a given vortex convection speed, K. Notice that variation of K influences the location of the flame response peak. Variation of ε scales the curves in magnitude. Variations in β and γ do not have significant influences on the results. This is important to understand as it helps guide which parameters require highly accurate measurements, and which do not. The corresponding phase result, shown in Figure 16b, shows even less variation across the different parametric combinations. Since phase is arbitrary, it is matched at $x/\lambda_c = 0.2$ where the experimental phase estimate is good.

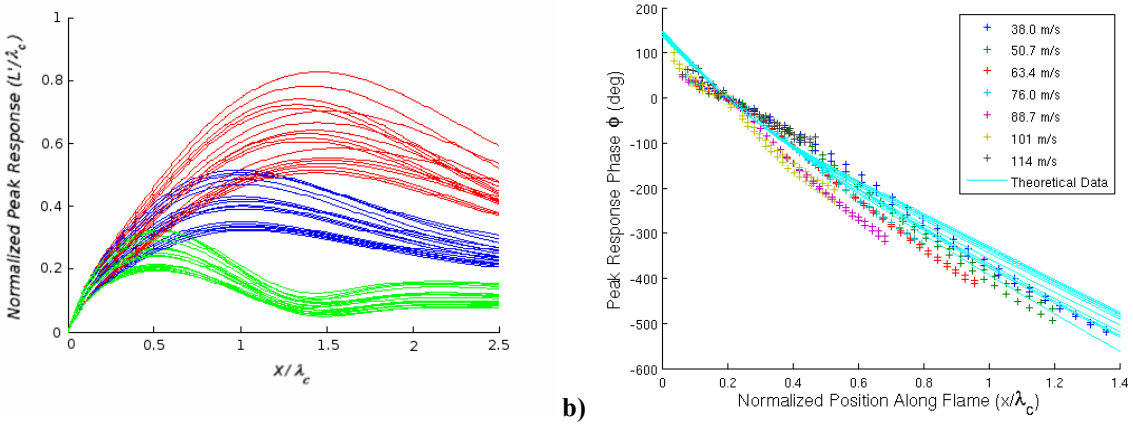

a) **b)**

Figure 16. a) Computation of flame sheet response gain over range of ε (-0.25 - 0.35), γ (3.4 - 4) and β (3.7 - 4.3) values at three different vortex convection speeds, K (red, K = 0.9, blue, K = 0.71, green, K = 0.58). b) Computation of flame sheet response phase over range of ε (-0.25-0.35), γ (3.4-4), β (3.7-4.3), and K (0.58-0.9) values combined with experimental results at 644K and various flow velocities (right flame edge only) at 12V excitation voltage.

Comparison of these gain and phase predictions with the measurements shows similar results. First, the gain results show the same rise, peaking, and then decay characteristics of the response curve. The phase curves show very similar linear variation with scaled downstream distance and, moreover, a similar insensitivity to variables other than downstream location, frequency, and mean flow velocities. This result is significant, as it shows that the basic model structure described here has the key built in physics to describe the flame response.

Given these points, it is useful to study further this solution of the G equation to further understand what factors influence these flame characteristics. This discussion closely follows Shanbhogue et al.[22] and Shin et al.[27] Consider first the initial growth region of the flame position magnitude. This initial increase in L' with y is due to the flame anchoring; i.e., regardless of the perturbation, the flame attachment point remains largely fixed. As such, the amplitude of L' must start from zero or near zero. It then rises with downstream distance in response to the fluctuating velocity field. Even if the flame attachment point vibrates some, i.e., $L'(y=0,t) \neq 0$, as long as the flame base does not move in phase and with the same amplitude as the flow field, similar behavior occurs. Furthermore, because the amplitude of fluctuations in the $y \sim 0$ region is so small, nonlinear effects are negligible. These nonlinear effects are contained in the following term in Eq. (2), which describes flame propagation normal to itself.

$$S_L \sqrt{\left(\frac{\partial L}{\partial x}\right)^2 + 1} \tag{4}$$

As such, the flame dynamics are described by a linearized G equation. An explicit solution for the slope of the $|L'(x,f_o)|$ vs. x curve can be derived from this linearized equation near the attachment point:

$$\frac{\partial \left|L'(x=0,f)\right|}{\partial x} = \frac{\left|u_n'(x=0,f)\right|}{u_t(x=0)} \frac{1}{\cos^2\theta} \tag{5}$$

This equation assumes that $L'(x=0, f) = 0$. It can be seen that the nearfield flame response slope increases linearly with perturbation magnitude and is a function of flame angle.

The peaking and subsequent reduction in amplitude of flame response in the "decay" region is the result of flame propagation normal to itself which destroys the flame wrinkles – a nonlinear effect[28]. Moreover, for a thermo-diffusively stable flame, unsteady curvature effects also work to destroy flame wrinkles – even at first order in perturbation amplitude – due to the increase in flame speed at locations concave to the flow and vice versa[29]. If the perturbation velocity persisted indefinitely downstream, at some point the flame wrinkle excitation and destruction processes would equilibrate, leading to a roughly constant (or oscillating) amplitude of flame perturbation with

downstream distance. However, because the amplitude of the excitation field decays with downstream distance, the amplitude of flame wrinkling decays.

IV. Conclusions

This paper has characterized the key parameters influencing the spatio-temporal response of an acoustically excited bluff body flame. Data and modeling results show that the flame response magnitude rises, peaks and then decays with downstream location. The phase of the flame response exhibits an essentially linearly decreasing dependence upon axial location. The kinematic model shows that the key processes controlling the response are 1) the anchoring of the flame at the bluff body, 2) the excitation of flame-front wrinkles by the oscillating velocity, and 3) flame propagation normal to itself at the local flame speed. The first two process control the growth of the flame response and the last process controls the decay.

These measurements and understanding provide valuable guidance for future experimental work. First, they show that line of sight imaging of flame response is not sufficient for quantitative comparisons of flame response gain; future measurements must utilize laser sheets to characterize the flame edge, as done in our earlier studies.[20-22] Second, they show that resolution of the bluff body nearfield is critical, in order to verify the flame anchoring which plays such an important role in the flame's nearfield response character. They also show provisions for increased downstream viewing will be needed to capture the "decay" region at the highest flow velocities. Finally, they show that accurate characterization of the vortex amplitude, propagation speed, and decay rate are needed to understand the sources of flame excitation.

Acknowledgments

The authors would like to thank the US Air Force for their financial support of this research (Contract FA-8650-07-M-2784).

References

[1]Smith, D. A. and Zukoski, E. E., "Combustion Instability Sustained by Unsteady Vortex Combustion", *21st AIAA/ASME/SAE/ASEE Joint Propulsion Conference and Exhibit*, 1985.

[2]Hegde, U. G., Reuter, D., Daniel, B. R. and Zinn, B. T., "Flame Driving of Longitudinal Instabilities in Dump Type Ramjet Combustors", *Combustion Science and Technology*, Vol. 55, No. 4, pp. 125-138.

[3]Poinsot, T. J., Trouve, A. C., Veynante, D. P., Candel, S. M. and Esposito, E. J., "Vortex-driven acoustically coupled combustion instabilities", *Journal of Fluid Mechanics*, Vol. 177, pp. 265-292.

[4]Yu, K. H., Trouvé, A. and Daily, J. W., "Low-frequency pressure oscillations in a model ramjet combustor", *Journal of Fluid Mechanics*, Vol. 232, pp. 47-72.

[5]Prasad, A. and Williamson, C. H. K., "The Instability of the Shear Layer Separating from a Bluff Body", *Journal of Fluid Mechanics*, Vol. 333, pp. 375-402.

[6]Sheridan, J., Soria, J., Wu, J. and Welsh, M. C., "The Kelvin-Helmholtz instability of the separated shear layer from a circular cylinder", *IUTAM Symposium*, Göttingen, Germany, 1992, pp. 115-118.

[7]Erickson, R. R., Soteriou, M. C. and Mehta, P. G., "The Influence of Temperature Ratio on the Dynamics of Bluff Body Stabilized Flames", *44th AIAA Aerospace Sciences Meeting & Exhibit*, Reno, Nevada, 2006.

[8]Hermanson, J. C. and Dimotakis, P. E., "Effects of Heat Release in a turbulent, reacting shear layer", *Journal of Fluid Mechanics*, Vol. 199, pp. 333-375.

[9]McMurtry, P. A., Riley, J. J. and Metcalfe, R. W., "Effects of heat release on the large-scale structure in turbulent mixing layers", *Journal of Fluid Mechanics*, Vol. 199, pp. 297-332.

[10]Soteriou, M. C. and Ghoniem, A. F., "The Vorticity Dynamics of an Exothermic, Spatially Developing, Forced Reacting Shear Layer", *Proceedings of the Combustion Institute*, Vol. 25, pp. 1265-1272.

[11]Wu, M. S. and Driscoll, J. F., "A numerical simulation of a vortex convected through a laminar premixed flame", *Combustion And Flame*, Vol. 91, No. 3-4, pp. 310-322.

[12]Sinibaldi, J. O., Mueller, C. J., Tulkki, A. E. and Driscoll, J. F., "Suppression of flame wrinkling by buoyancy - The baroclinic stabilization mechanism", *AIAA Journal*, Vol. 36, No. 8, pp. 1432-1438.

[13]Louch, D. S. and Bray, K. N. C., "Vorticity in unsteady premixed flames: vortex pair–premixed flame interactions under imposed body forces and various degrees of heat release and laminar flame thickness", *Combustion And Flame*, Vol. 125, No. 4, pp. 1279-1309.

[14]Ducruix, S., Schuller, T., Durox, D. and Candel, S., "Combustion dynamics and instabilities: Elementary coupling and driving mechanisms", *Journal of Propulsion and Power*, Vol. 19, No. 5, pp. 722-734.

[15]Preetham, Thumuluru, S. K. and Lieuwen, T., "Linear Response of Premixed Flames to Flow Oscillations: Unsteady Stretch Effects", *AIAA Aerospace Sciences Meeting and Exhibit*, Reno, NV, 2007.

[16]Schuller, T., Durox, D. and Candel, S., "A unified model for the prediction of laminar flame transfer functions comparisons between conical and V-flame dynamics", *Combustion And Flame*, Vol. 134, No. 1-2, pp. 21-34.

[17]Preetham and Lieuwen, T., "Nonlinear Flame-Flow Transfer Function Calculations: Flow Disturbance Celerity Effects", *40th AIAA/ASME/SAE/ASEE Joint Propulsion Conference & Exhibit*, 2004.

[18]Preetham and Lieuwen, T., "Nonlinear Flame-Flow Transfer Function Calculations: Flow Disturbance Celerity Effects Part 2", *43rd AIAA Aerospace Sciences Meeting & Exhibit*, 2005.

[19]Peters, N., *Turbulent Combustion*, Cambridge University Press, 2000.

[20]Shanbhogue, S. J. and Lieuwen, T., "Response of a Rod Stabilized, Premixed Flame to Longitudinal Acoustic Forcing", *ASME Turbo Expo: Power for Land, Sea and Air*, Barcelona, Spain, 2006.

[21]Shanbhogue, S. J., Plaks, D., Nowicki, G., Preetham and Lieuwen, T., "Response of Rod Stabilized Flames to Harmonic Excitation: Shear Layer Rollup and Flame Kinematics", AIAA# 2006-5232, 2006.

[22]Shanbhogue, S. J., Shin, D.-H., Hemchandra, S., Plaks, D. and Lieuwen, T., "Flame-sheet dynamics of bluff-body stabilized flames using longitudinal acoustic forcing", *Proceedings of the Combustion Institute*, 2009, doi:10.1016/j.proci.2008.06.034.

[23]Brown, C. T., McDonell, V. G. and Kiel, B., "Test Bed for Characterization of Liquid Jet Injection Phenomenon at Augmentor Conditions", AIAA# 2006-4569, 2006.

[24]Shanbhogue, S. J. and Lieuwen, T., "Studies on the Vorticity Field of Harmonically Excited Bluff Body Flames", AIAA# 2008-122, 2008.

[25]Jiang, G. and Peng, D., "Weighted ENO Schemes for Hamilton-Jacobi Equations", *SIAM Journal on Scientific Computing*, Vol. 21, pp. 2126-2143.

[26]Gottlieb, S. and Shu, C., "Total Vatiation Diminishing Runge-Kutta Schemes", *Mathematics of Computation*, Vol. 67, pp. 73-85.

[27]Shin, D.-H., Shanbhogue, S. J. and Lieuwen, T., "Premixed Flame Kinematics in an Axially Decaying, Harmonically Oscillating Vorticity Field", AIAA# 2008-5042, 2008.

[28]Law, C. K. and Sung, C. J., "Structure, Aerodynamics and Geometry of Premixed Flamelets", *Progress in Energy and Combustion Science*, Vol. 26, No. 4-6, pp. 459-505.

[29]Preetham, Thumuluru, S. K. and Lieuwen, T., "Response of Premixed Flames to Flow Oscillations: Unsteady Curvature Effects", AIAA# 2006-960, 2006.